ELECTRONIC SUPPLEMENTARY INFORMATION

Pathways towards managing cost and degradation risk of fast charging cells with electrical and thermal controls

Juhyun Song[†,*], Zhe Liu[†], Kevin W. Knehr[*], Joseph J. Kubal, Hong Keun Kim, Dennis W. Dees, Paul A. Nelson, Shabbir Ahmed

Chemical Science and Engineering Division

Argonne National Laboratory, Lemont, IL 60439, USA.

[†] These authors contributed equally

Corresponding authors: jusong@apple.com (J.S.), knehrkw@anl.gov (K.W.K)

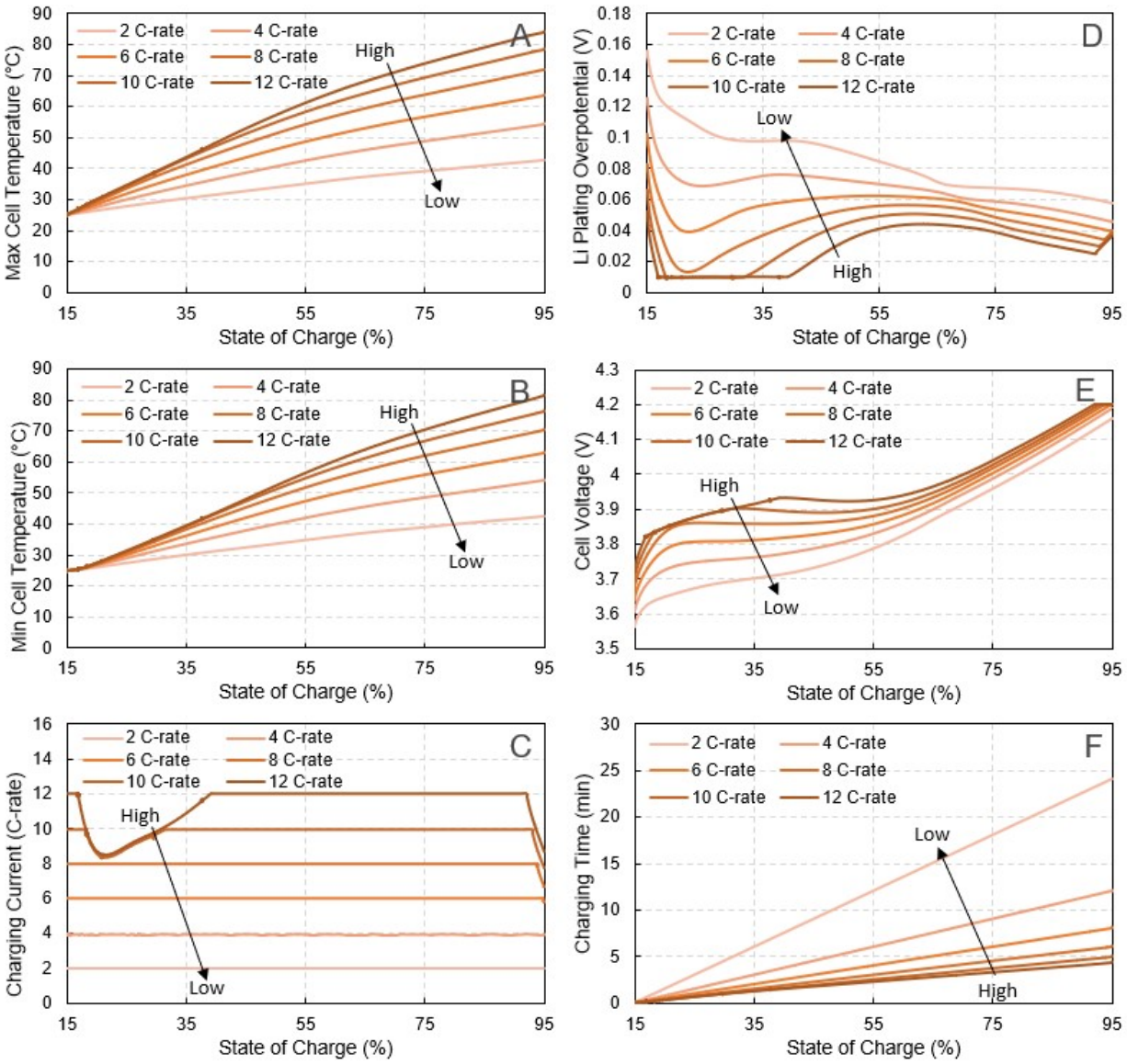

Figure S1. Zero Thermal Management (adiabatic condition), related to Figure 2.

Charging curves of different current C-rates for the 60 μm anode thickness cell, using an initial temperature (T_0) of 25 °C, an overpotential cutoff (η_{pp}) of 10 mV for lithium plating protection, and an upper cutoff voltage ($E_{cell,lim}$) of 4.2 V: (A) maximum cell local temperature (T_{max}), (B) anode Li plating overpotential (η), (C) minimum cell local temperature (T_{min}), (D) cell voltage (E_{cell}), (E) max charging current limit (I_{lim}) in C-rate, and (F) charging time, versus cell state of charge, respectively. For the scenarios presented here, the cell maximum temperature during charging was as high as 85 °C using 12C-rate as the maximum charging current limit, as shown in (A). With elevated cell temperature, the anode overpotential is substantially pushed above the Li plating overpotential cutoff (η_{pp} = 10mV), as shown in (B). Constant current charging from SOC 15% to 95% without triggering Li plating protection can be achieved with up to 8C-rate as maximum current limit.

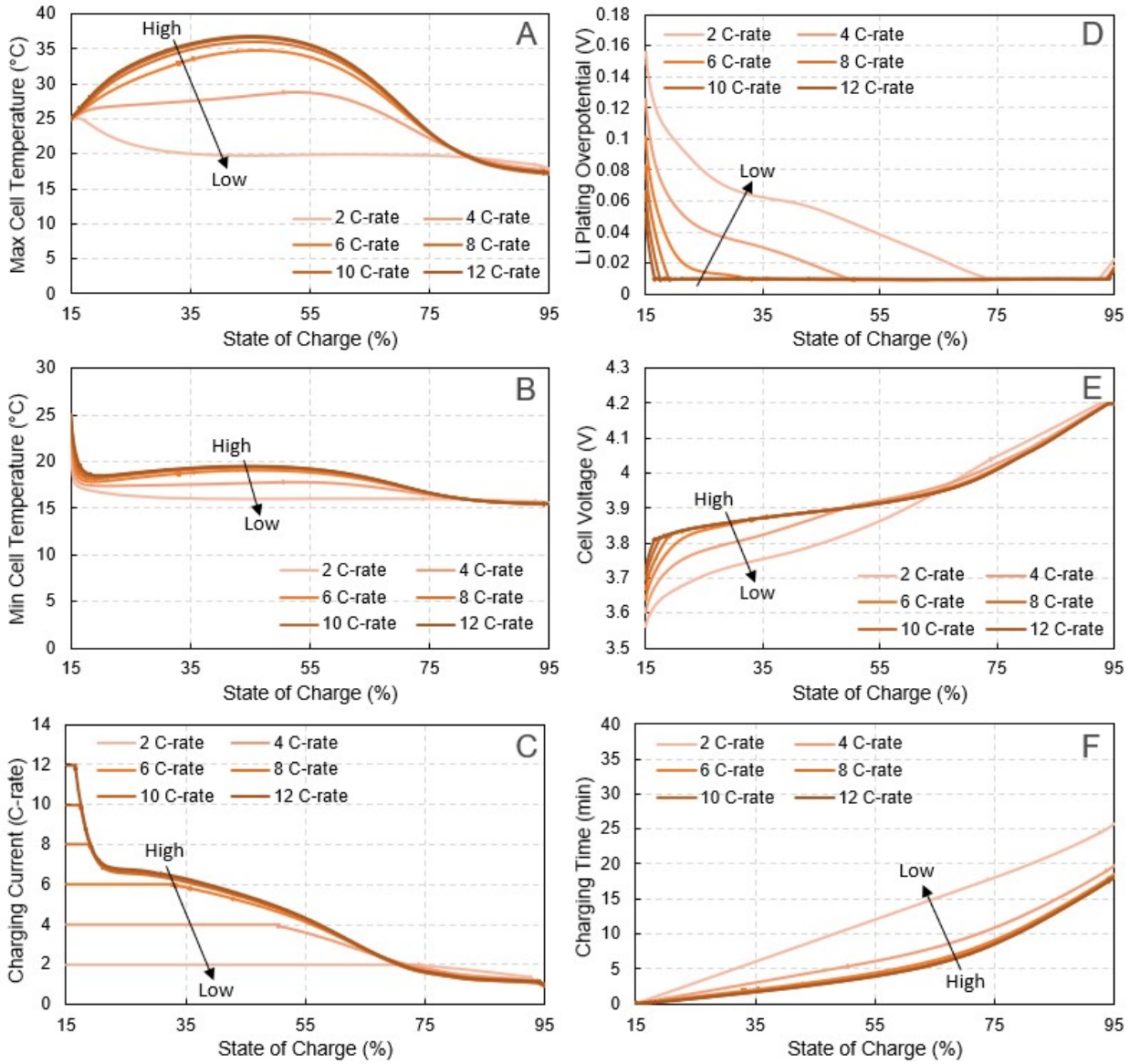

Figure S2. Constant Thermal Management (constant cooling condition), related to Figure 2.

Charging curves of different current C-rates for the 60 μm anode thickness cell, using an initial temperature (T_0) of 25 °C, a coolant temperature (T_{clnt}) of 15 °C**,** an overpotential cutoff (η_{pp}) of 10 mV for lithium plating protection, and an upper cutoff voltage ($E_{cell,lim}$) of 4.2 V: (A) maximum cell local temperature (T_{max}), (B) anode Li plating overpotential (η), (C) minimum cell local temperature (T_{min}), (D) cell voltage (E_{cell}), (E) max charging current limit (I_{lim}) in C-rate, and (F) charging time, versus cell state of charge, respectively. A constant coolant flow of 15 °C and 6.8 kg/(m²·s), directly cooling the type-'a' surfaces of the cell and the edge of cooling plate, is applied from the beginning of charging. Therefore, the cell maximum temperature during charging is well below 40 °C for 2 to 12C-rate as the maximum charging current limit, as shown in (A). Due to the lowered cell temperature, the anode overpotential quickly drops to the Li plating overpotential cutoff (η_{pp} = 10mV), and Li plating protection mode is activated by maintaining anode overpotential at the cutoff limit, as shown in (B).

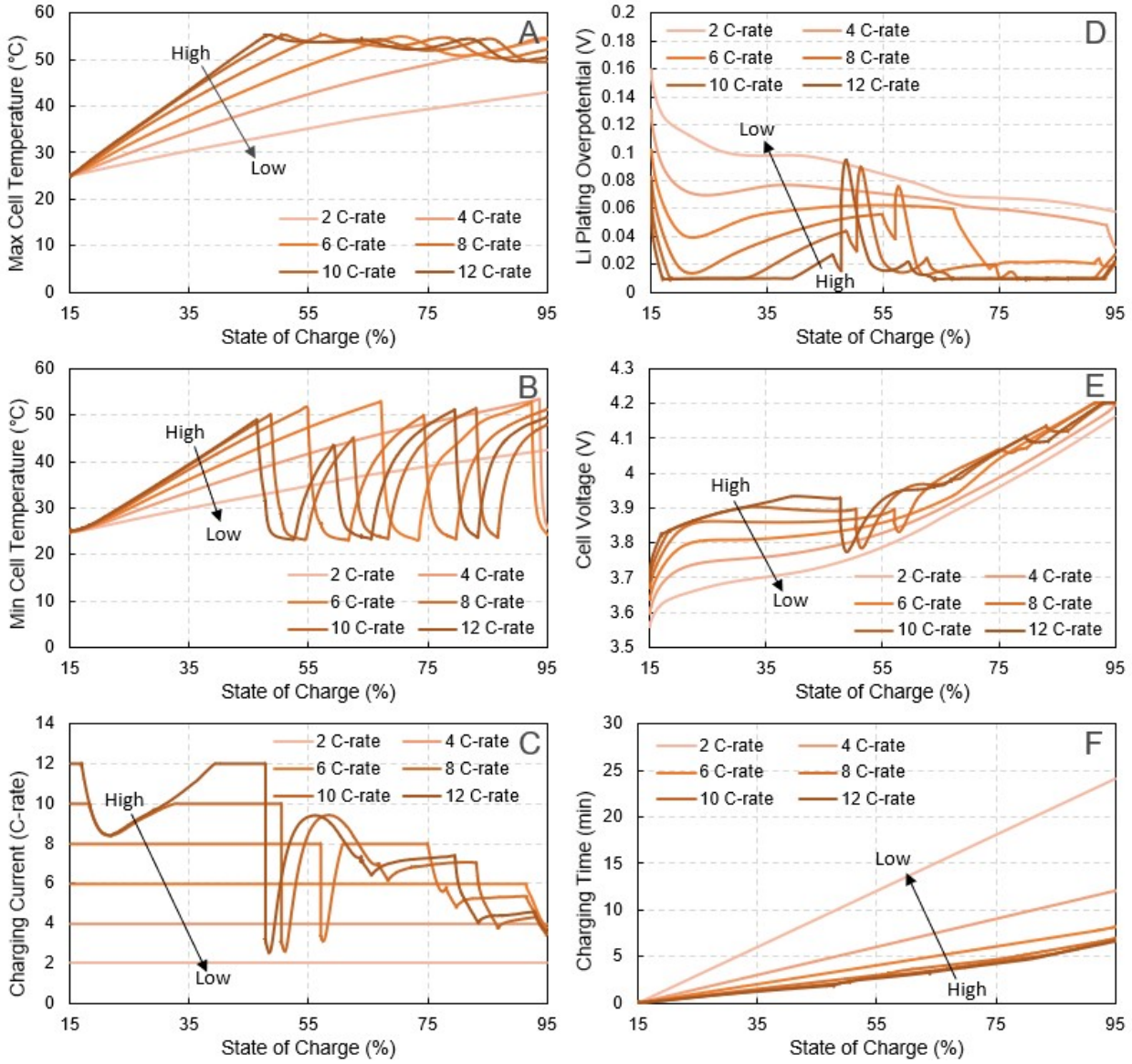

Figure S3. Active Thermal Management (actively controlled cooling), related to Figure 2.

Charging curves of different current C-rates for the 60 μm anode thickness cell, using an initial temperature (T_0) of 25 °C, a coolant temperature (T_{clnt}) of 15 °C**,** a maximum allowable temperature ($T_{max,lim}$) of 55 °C with the coolant flow triggered (on/off) at 54 °C, an overpotential cutoff (η_{pp}) of 10 mV for lithium plating protection, and an upper cutoff voltage ($E_{cell,lim}$) of 4.2 V: (A) maximum cell local temperature (T_{max}), (B) anode Li plating overpotential (η), (C) minimum cell local temperature (T_{min}), (D) cell voltage (E_{cell}), (E) max charging current limit (I_{lim}) in C-rate, and (F) charging time, versus cell state of charge, respectively. A coolant flow of 15 °C and 6.8 kg/(m²·s) is actively controlled by being turned on/off when cell maximum temperature approaches (1°C below) the upper limit, or $T_{max,lim}$ = 55 °C. As such, the cell maximum temperature will be eventually maintained at around $T_{max,lim}$ = 55 °C, as shown in (A). With the elevated, yet controlled, cell temperature, the anode overpotential is effectively raised above the Li plating overpotential cutoff (η_{pp} = 10mV). Consequently, the charging time needed is substantially shortened (compared to S2), as shown in (F).

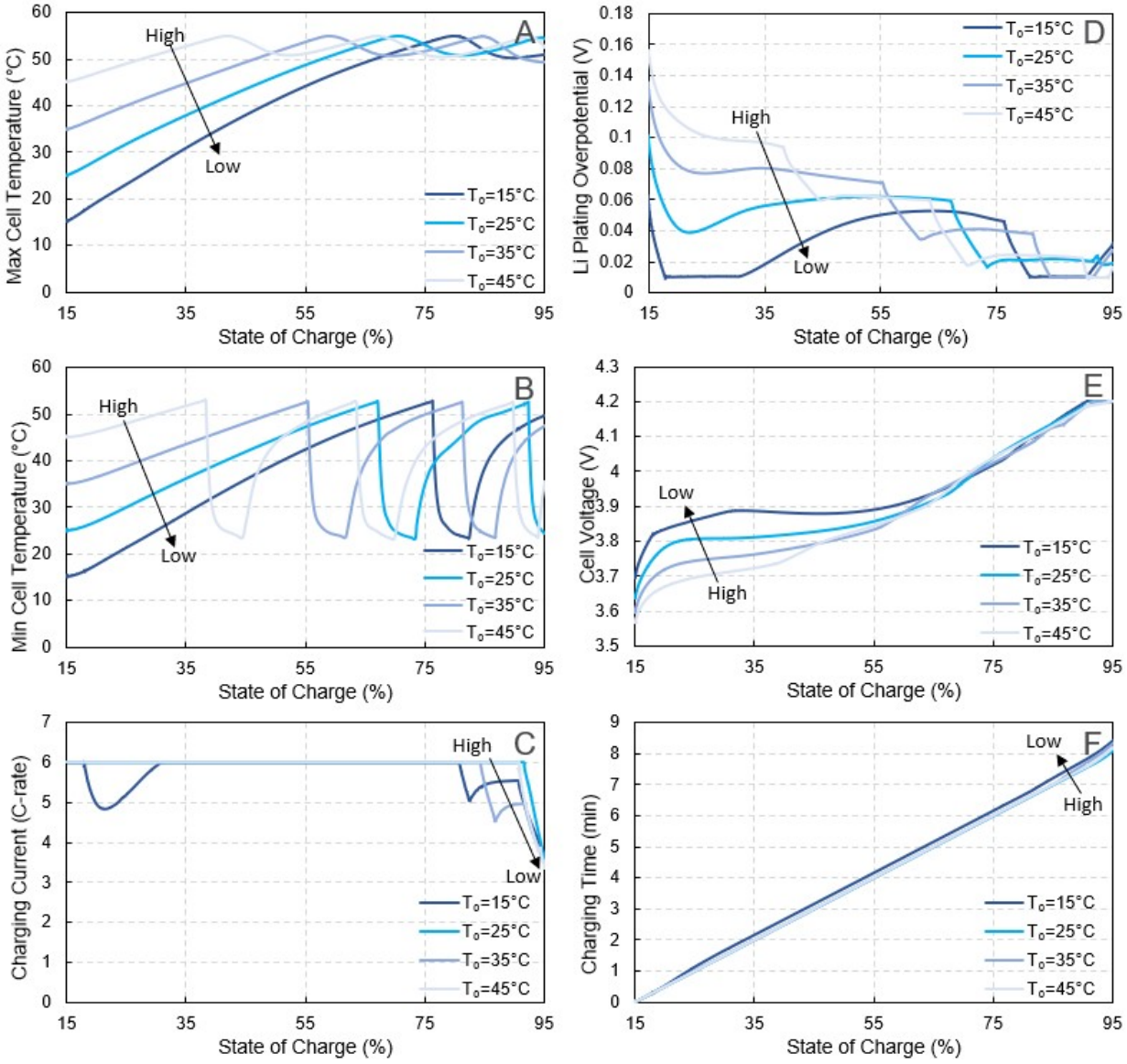

Figure S4. Influence of initial temperature on charging, related to Figure 3.

Active Thermal Management charging curves of initial temperatures (T_0) ranging from 15 °C to 45 °C, using a 60 µm anode thickness cell, a coolant temperature (T_{clnt}) of 15 °C, a maximum allowable temperature ($T_{max,lim}$) of 55 °C with the coolant flow triggered (on/off) at 54 °C, an overpotential cutoff (η_{pp}) of 10 mV for lithium plating protection, max current limit (I_{lim}) of 6C, and an upper cutoff voltage ($E_{cell,lim}$) of 4.2 V: (A) maximum cell local temperature (T_{max}), (B) anode Li plating overpotential (η), (C) minimum cell local temperature (T_{min}), (D) cell voltage (E_{cell}), (E) max charging current limit (I_{lim}) in C-rate, and (F) charging time, versus cell state of charge, respectively.

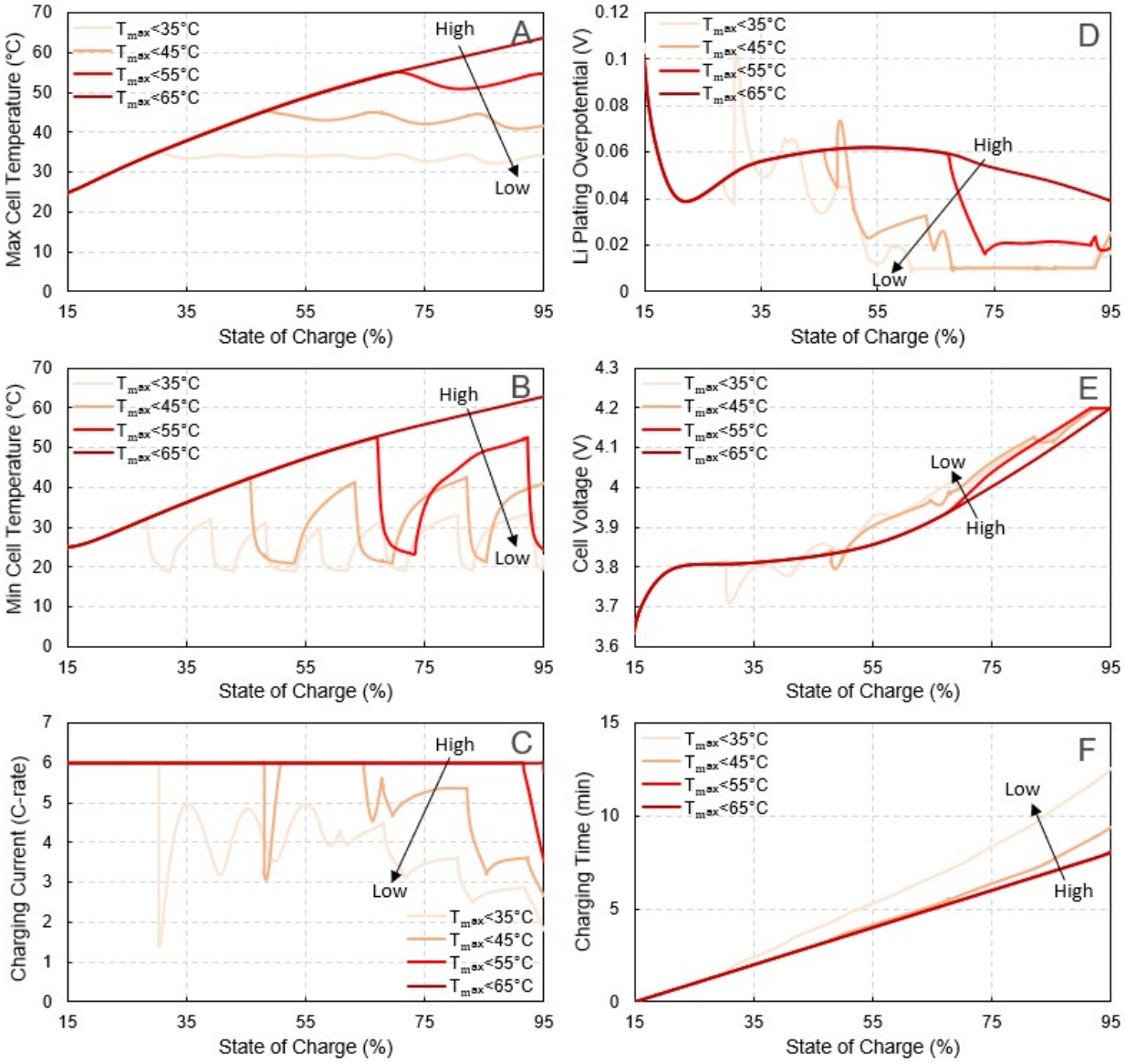

Figure S5. Influence of $T_{max,lim}$ on charging, related to Figure 3.

Active Thermal Management charging curves of maximum temperature limits ($T_{max,lim}$) ranging from 35 °C to 65 °C, using a 60 µm anode thickness cell, an initial temperature (T_0) of 25 °C, a coolant temperature (T_{clnt}) of 15 °C with the coolant flow triggered (on/off) at 54 °C, an overpotential cutoff (η_{pp}) of 10 mV for lithium plating protection, max current limit (I_{lim}) of 6C, and an upper cutoff voltage ($E_{cell,lim}$) of 4.2 V: (A) maximum cell local temperature (T_{max}), (B) anode Li plating overpotential (η), (C) minimum cell local temperature (T_{min}), (D) cell voltage (E_{cell}), (E) max charging current limit (I_{lim}) in C-rate, and (F) charging time, versus cell state of charge, respectively.

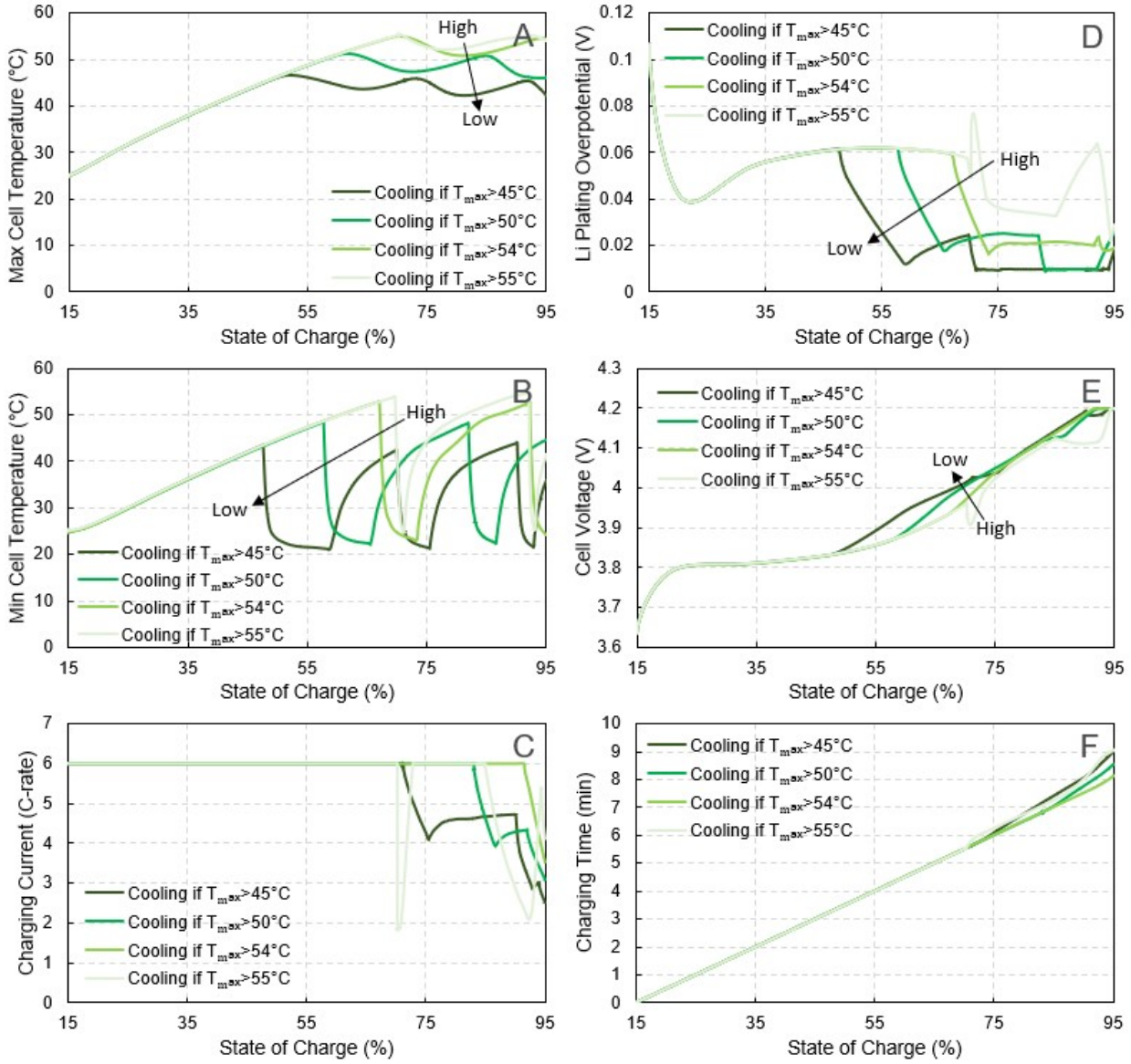

Figure S6. Influence of coolant triggering temperature on charging, related to Figure 3.

Active Thermal Management charging curves of coolant triggered temperatures ranging from 45 °C to 55 °C, using a 60 µm anode thickness cell, an initial temperature (T_0) of 25 °C, a coolant temperature (T_{clnt}) of 15 °C, a maximum allowable temperature ($T_{max,lim}$) of 55 °C, an overpotential cutoff (η_{pp}) of 10 mV for lithium plating protection, max current limit (I_{lim}) of 6C, and an upper cutoff voltage ($E_{cell,lim}$) of 4.2 V: (A) maximum cell local temperature (T_{max}), (B) anode Li plating overpotential (η), (C) minimum cell local temperature (T_{min}), (D) cell voltage (E_{cell}), (E) max charging current limit (I_{lim}) in C-rate, and (F) charging time, versus cell state of charge, respectively.

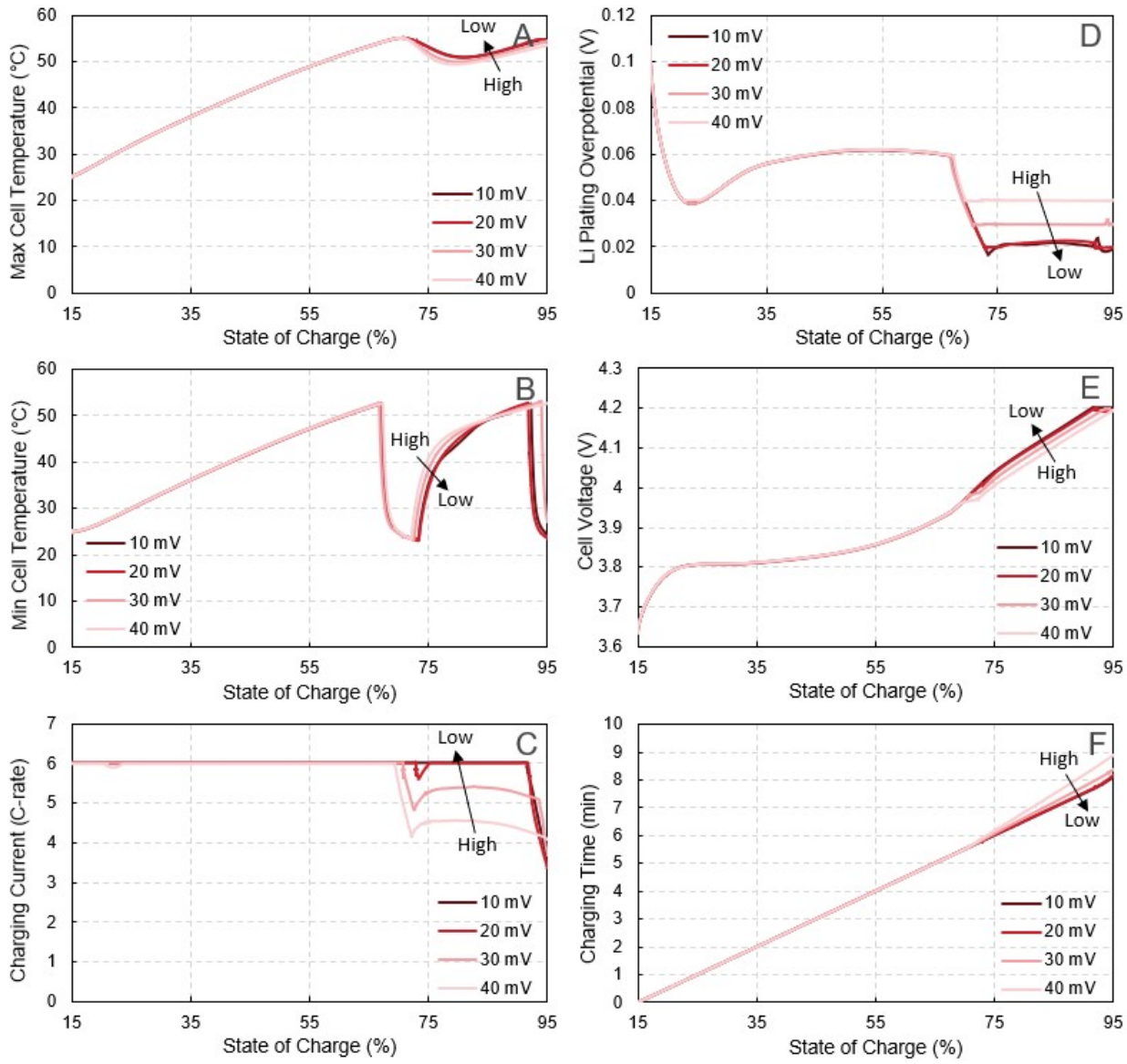

Figure S7. Influence of cutoff potential on charging, related to Figure 3.

Active Thermal Management charging curves of overpotential cutoff (η_{pp}) for lithium plating protection ranging from 10 to 40 mV, using a 60 µm anode thickness cell, an initial temperature (T_0) of 25 °C, a coolant temperature (T_{clnt}) of 15 °C**,** a maximum allowable temperature ($T_{max,lim}$) of 55 °C with the coolant flow triggered (on/off) at 54 °C, , max current limit (I_{lim}) of 6C, and an upper cutoff voltage ($E_{cell,lim}$) of 4.2 V: (A) maximum cell local temperature (T_{max}), (B) anode Li plating overpotential (η), (C) minimum cell local temperature (T_{min}), (D) cell voltage (E_{cell}), (E) max charging current limit (I_{lim}) in C-rate, and (F) charging time, versus cell state of charge, respectively.

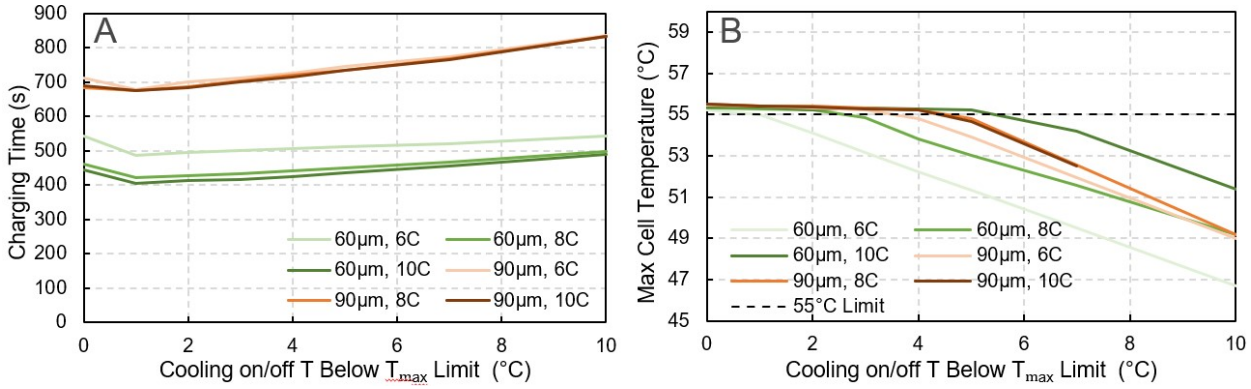

Figure S8. Sensitivity analyses of cooling on/off temperature, related to Figure 3.

Simulations run using Active Thermal Management conditions with a coolant temperature (T_{clnt}) of 15 °C, a maximum allowable temperature ($T_{max,lim}$) of 55 °C, an overpotential cutoff (η_{pp}) of 10 mV for lithium plating protection, and an upper cutoff voltage ($E_{cell,lim}$) of 4.2 V: (A) coolant flow triggered (on/off) temperature impact on charging time for selected cell anode thicknesses and charging current C-rates using an initial temperature (T_0) of 25 °C, (B) coolant flow triggered (on/off) temperature impact on maximum cell temperature during charging for selected cell anode thicknesses and charging current C-rates using an initial temperature (T_0) of 25 °C. (A) demonstrates that the shortest charging time is achieved by using a coolant flow on/off temperature 1°C below $T_{max,lim}$. (B) demonstrates that the maximum cell temperature limit can be reached (the cell is not over-cooled) during charging by using coolant flow on/off temperature in the range of 0-5 below $T_{max,lim}$. Combining (A) and (B) the optimal coolant flow on/off temperature, which achieves the shortest charging time while fully taking advantage of the cell thermal window, is 1°C below $T_{max,lim}$.

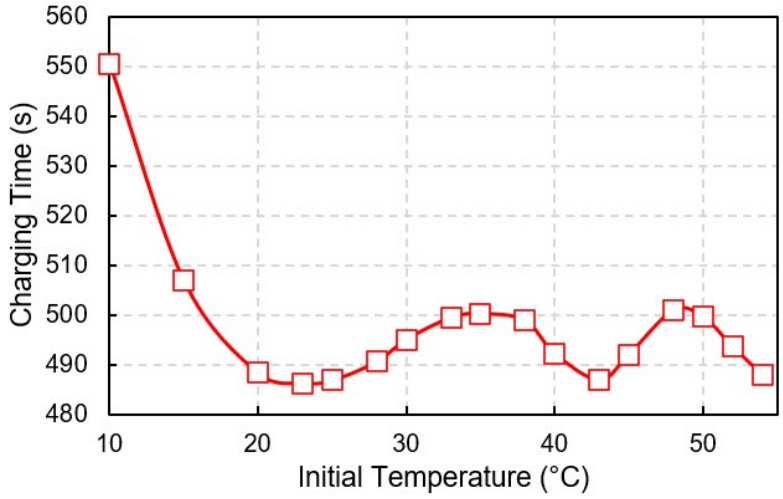

Figure S9. Oscillatory behavior of charge time with respect to initial temperature, related to Figure 3.

Charging times for the Active Thermal Management with different initial temperatures (T_0), using a 60 µm anode thickness cell, a coolant temperature (T_{clnt}) of 15 °C**,** a maximum allowable temperature ($T_{max,lim}$) of 55 °C with the coolant flow triggered (on/off) at 54 °C, an overpotential cutoff (η_{pp}) of 10 mV for lithium plating protection, max current limit (I_{lim}) of 6C, and an upper cutoff voltage ($E_{cell,lim}$) of 4.2 V. Results indicate initial cell temperatures higher than 15°C have similar charging times, since the cell temperature rises rapidly during ATM fast-charging. It is also observed an oscillated charging time (within 15 s) with increased initial temperature, which is due to the on/off control algorithm and heat transfer latency within the cell.

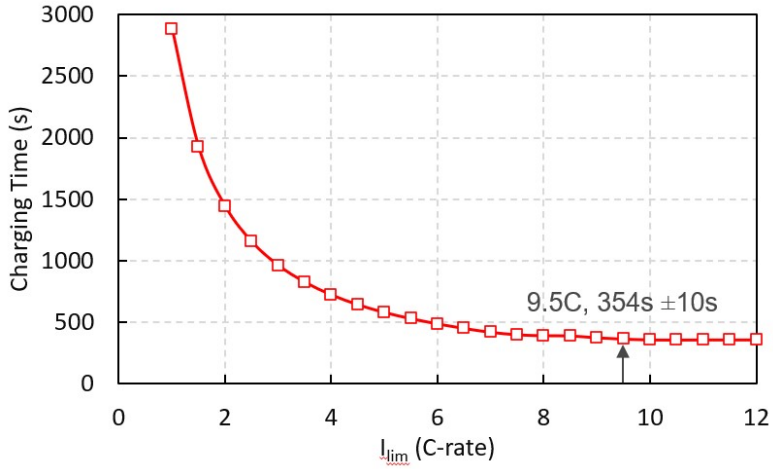

Figure S10. Screening method for determining $I_{lim,min}$, related to Figure 5.

Demonstration of the screening method for determining the lowest I_{lim} to achieve the minimum charging time based on the charge time vs. maximum charging current (C-rate) plot of a 54-µm anode thickness using $T_{max,lim}$ = 55 °C, η_{pp} = 10 mV, and the set of degradation current limits. The current reported in Figure 5 corresponds to the lowest C-rate that achieves a charging time within 10s of the lowest reported value within the 1 to 12C range. In this example, this corresponds to a 9.5C $I_{lim,min}$ to achieve a minimum charging time of 354s (~6min).

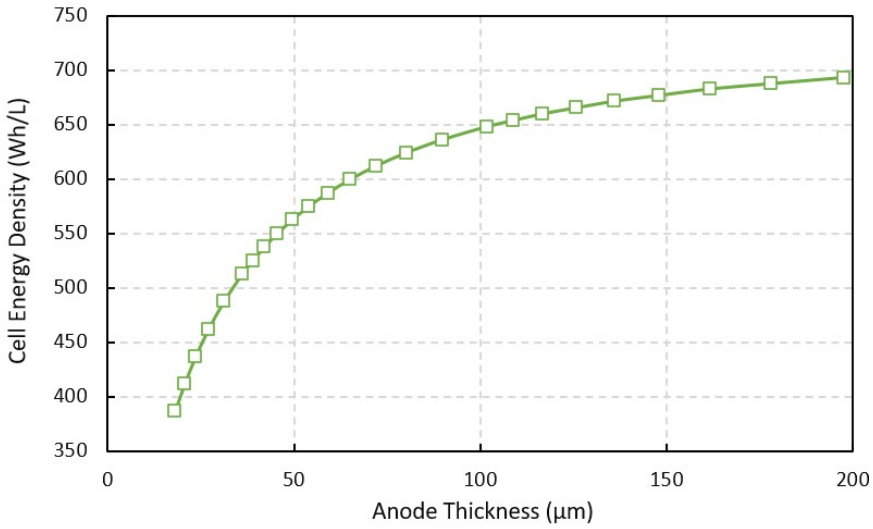

Figure S11. Cell energy density vs. anode thickness correlation based on BatPaC database, related to Figure 5.

Energy density was calculated with an anode composition of 98:2 wt% of graphite and binder, respectively, and a cathode composition of 96:2:2 wt% NMC532, carbon additive, binder, respectively. The Cu current collector, Al current collector, and separator were 10, 16, and 20 µm thick. Default values from BatPaC v4.0 were used for all other parameters. See section "BatPaC Cost and Energy Density Modeling" below and tabulated values in Table S5 for more information.

Modeling Details

All simulations in this work were performed by COMSOL Multiphysics 5.5 with Livelink to MATLAB R2020a. As briefed in the main text "Model Description" section, the charging process of a cell in a battery pack environment with thermal management system was simulated by a homogenized 3-D continuum model, which includes two 1-D electrochemical models and a 3-D thermal model. The governing equations, boundary conditions, and parameters for all three models are provided in Tables S1-S4 below. The homogenized model was developed based on the assumption that the cell charging rate is limited by overheating (maximum cell temperature, T_{max}) and Li plating (anode overpotential, η) only, as elaborated in the main text "Introduction" section. The simulations were realized by coupling the Lithium-Ion Battery Module and the Heat Transfer Module and integrating with PDEs/ODEs (partial/ordinary differential equations, respectively) and Event Controllers within COMSOL. In the time-dependent solver, a tolerance factor of 0.01 was used for electric potential calculations, while tolerance factors of 0.1 were applied for the other variables. This model is validated to a fully coupled 3D electrochemical thermal model.[1]

Electrochemical Model

The electrochemical model uses the Newman pseudo-2D formulation implemented by the Lithium-Ion Battery Module in COMSOL.[2] Two 1-D electrochemical Newman models are simulated in the homogenized 3-D model. The first one is solved at cell average temperature, T_{avg}, which calculates the heat generation rate (input to 3-D thermal model) and the overall electrochemistry of the cell. The second 1-D model is solved at cell minimum temperature, T_{min}, which predicts the onset of lithium plating based on the anode overpotential, η, and provides feedback to the PID controller for plating protection (see Equation 21 in Tables S2). The constant risk charging algorithm is applied on the T_{avg} model via boundary conditions of Equation 16, 17, 18, 21 and 22. The T_{min} model is connected to the T_{avg} model by assuming zero voltage drop in the current collectors, or the same cell voltage E_{cell}. The cell average and minimum temperatures during charging are received from the 3-D thermal model. In this work, NMC 532 was used as the cathode material with usable capacity range of 0.24 to 0.91, and graphite A12 was used as the anode material with usable capacity range of 0.016 to 0.87 (both ranges are expressed by lithium intercalation fraction). Their corresponding open-circuit voltage curves are shown in Figure S12 below, which were measured in Gen 2 electrolyte (see Table S3) with respect to a lithium metal counter electrode.

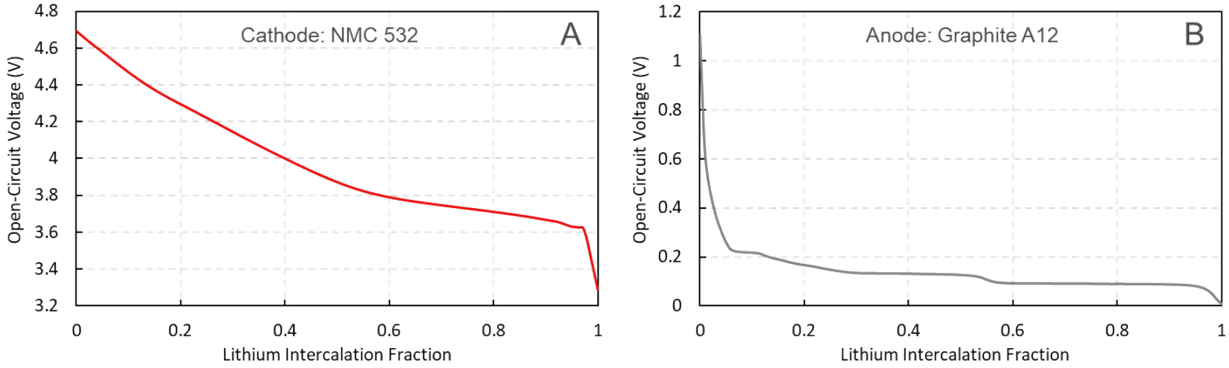

Figure S12. C/20 discharge data used to approximate open circuit voltage in the model.

Thermal Model

The 3-D thermal model takes in the heat generation rate from the electrochemical model, and simulates the temperature distribution and evolution during charging within a cell in a battery pack environment with thermal management system. The heat transfer within the 3-D cell, solved by Equation 12 (Table S1), was realized by the Heat Transfer in Solids Module in COMSOL. The total heat generation rate, expressed by Equation 13 (Table S1), includes electrochemical heating from the reaction and transport within the cell (calculated based on the electrochemical model at T_{avg}) and the Joule heating from current collectors (calculated based on charging current and resistance). The thermal management system was simplified by simulating the coolant in channel in contact with cell type-'a' surfaces (see Figure 1), with a uniform coolant temperature distribution. The coolant flow rate in channel (when thermal protection mode is activated) is 6.8 kg/(m²·s) with an invariant incoming/fresh coolant temperature of 15 °C. The heat transfer in coolant was solved by Equation 14 (Table S2). Overall, the heat conductions within the 3-D cell and the channel coolant were linked through the boundary condition at the type-'a' surfaces, expressed by Equation 23 (Table S2).

The thermal model solves the temperature distribution at each time step and passes (1) the minimum cell temperature to the T_{min} electrochemical model for anode overpotential estimation and Li plating protection, (2) the average cell temperature to the T_{avg} electrochemical model for the overall cell electrochemistry and the next time step heat generation rate calculation, and (3) the maximum cell temperature T_{max} to the thermal protection PID controller to prevent overheating by tuning charging current based on Equation 22 (Table S2).

Validation of the Homogenized 3-D Model

The applicability of the homogenized 3-D electrochemical-thermal model was validated by a comparison with a fully coupled 3-D multi-scale multi-domain (MSMD) model.[1] Their cell voltage and maximum temperature evolutions during 1C to 4C discharging rates are shown in good agreement with each other as illustrated by figure (a) and (b) below, respectively.

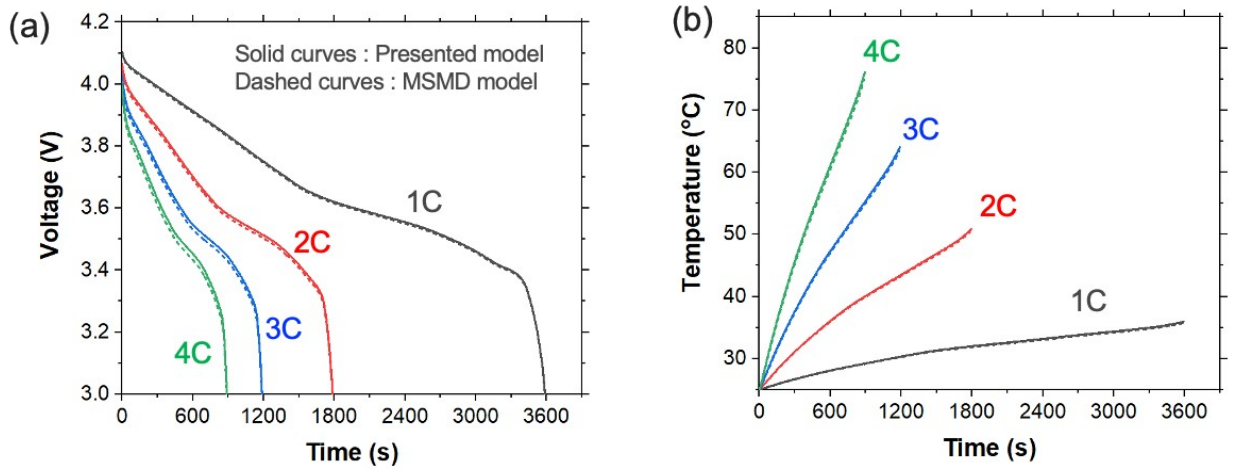

Figure S13. Comparison of present model with previously published MSMD model.[1,3]

Constant-Risk Charging Protocol

Enabled by the Event Controllers and ODEs in COMSOL, the constant-risk fast charging protocol minimizes the charging time by fully taking advantage of the cell electrochemical-thermal window and the charging current limit. Using a PID controller, the temporal charging current is actively tuned to maintain at the lowest anode overpotential as well as highest cell temperature allowable. This protocol is used in all simulations regardless of the cooling scenario. As demonstrated by Figure S14, the process starts with constant current charging at the maximum allowed current. This pre-selected maximum charging current in the initial stage is based on both cell design and charger capability. The cell is charged from the initial 15% state of charge (SOC) to the upper end of 95% in all cases, using the constant current mode unless one of the three criteria is met: (1) the cell voltage reaches the upper voltage limit, i.e. $E_{cell,lim}$, (2) the anode overpotential drops below the Li plating overpotential limit, i.e. η_{pp}, or (3) the highest local temperature in the cell rises beyond the maximum temperature limit, i.e. $T_{max,lim.}$ In case (1), constant voltage mode will be activated and the charging boundary condition will be switched to an invariant applied cell voltage or $E_{cell,lim}$. In case (2), Li plating protection mode will be activated with the charging current tuned by the PID controller to keep the anode overpotential at the lower bound or η_{pp}. In case (3), thermal protection mode will be activated with the charging current regulated by the PID controller to keep the highest cell local temperature below the maximum allowed value or $T_{max,lim}$. During the entire charging process, the maximum current protection will always be online to guarantee the applied current does not exceed the current limit. Charging ends when the cell SOC reaches 95%.

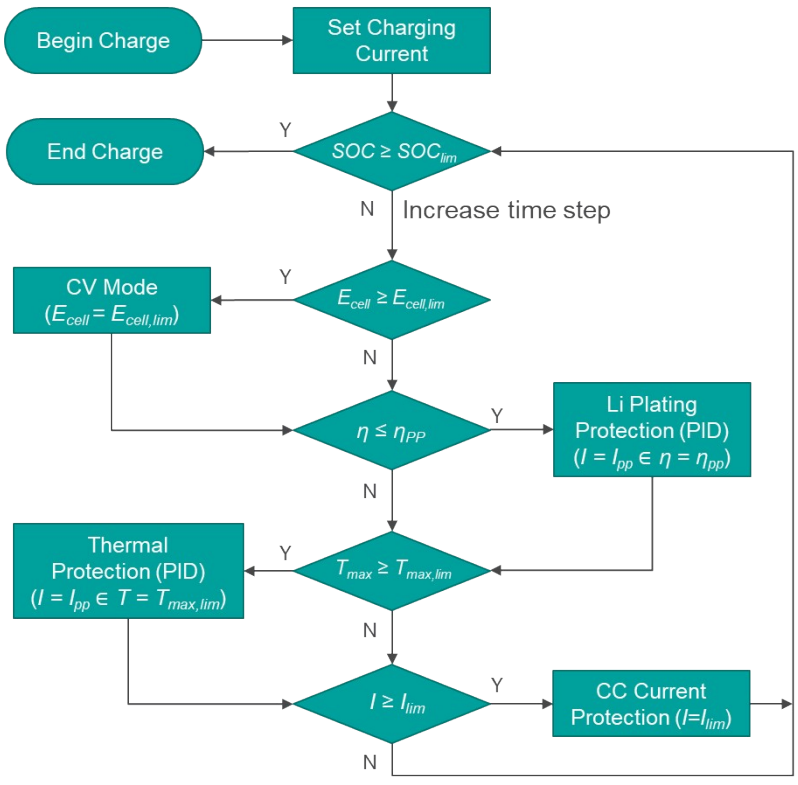

Figure S14. Flow chart depicting constant risk charging protocol.

BatPaC Cost and Energy Density Modeling

BatPaC version 4.0 was used to compute the costs and energy densities of cells.[4] Using the default parameters for the NMC 532 and graphite couple, the N:P ratios (from 1.1 to 1.33) were adjusted to ensure that the model had the corresponding anode and cathode thicknesses that were utilized in the COMSOL model. Other changes away from the default were the Al current collector thickness (15 to 16μm), the separator thickness (15 to 20 μm), and the separator void fraction increasing from 39% to 50%. The electrode compositions were 98:2 wt% of graphite and binder for the anode, respectively, and 96:2:2 wt% NMC532, carbon additive, binder, for the cathode, respectively. A porosity of 25% was used for both electrodes. From this, the cell capacities were adjusted so the cell dimensions were within 1% of 30x10x2 cm cells that were used for the COMSOL model. The cost versus thickness curve was then obtained by repeating this process for the series of anode thicknesses used in this study. The cost is on a $/cell level for a 100,000 pack per year production volume, with each pack containing 400 cells of this size. The cost on a cell level does not include pack level components (i.e. pack casing, BMU).

Table S1. Governing equations for 1D electrochemical model and 3D thermal model.

Equation No.	Expression	Description
1D Electrochemical Model Governing Equations		
1	$\varepsilon_l \frac{\partial c_l}{\partial t} = \varepsilon_l \frac{\partial}{\partial x}\left(D_{l,eff} \frac{\partial c_l}{\partial x}\right) - \frac{i_l \partial t_+}{F \partial x} + \frac{(1-t_+)\partial i_l}{F \partial x}$	Diffusion in concentrated solution electrolyte
2	$i_l = -\sigma_{l,eff} \frac{\partial \phi_l}{\partial x} + \left(\frac{2\sigma_{l,eff} RT}{F}\right)\left(1 + \frac{\partial ln f_{\pm}}{\partial ln c_l}\right)(1-t_+)\frac{\partial ln c_l}{\partial x}$	Ohm's law for concentrated solution electrolyte
3	$\frac{\partial i_l}{\partial x} = a_v (i_{loc} + i_{dl})$	Current in electrolyte
4	$i_{loc} = i_0\left(\exp\left(\frac{\alpha_a F \eta}{RT}\right) - \exp\left(\frac{-\alpha_c F \eta}{RT}\right)\right)$	Butler-Volmer equation representing electrochemical reaction at solid/liquid interfaces
5	$i_{dl} = \left(\frac{\partial(\phi_s - \phi_l)}{\partial t}\right) C_{dl}$	Double layer current
6	$\eta = \phi_s - \phi_l - E_0^{eq}$	Activation overpotential
7	$i_0 = i_{0,ref}\left(\frac{c_s}{c_{s,ref}}\right)^{\alpha_c}\left(\frac{c_{s,max} - c_s}{c_{s,max} - c_{s,ref}}\right)^{\alpha_a}\left(\frac{c_l}{c_{l,ref}}\right)^{\alpha_a}$	Exchange current density
8	$\frac{\partial c_s}{\partial t} = \frac{1}{r^2}\frac{\partial}{\partial r}\left(D_s r^2 \frac{\partial c_s}{\partial r}\right)$	Diffusion in electrode particle
9	$i_s = -\sigma_{s,eff} \frac{\partial \phi_s}{\partial x}$	Ohm's law
10	$\frac{\partial i_l}{\partial x} + \frac{\partial i_s}{\partial x} = 0$	Charge conservation
11	$X_{eff} = \varepsilon^p X$	Effective parameters (X = D_l, σ_l, σ_s)
3D Thermal Model Governing Equations		
12	$\rho_{cell} C_{p,cell} \frac{\partial T}{\partial t} + \nabla \cdot (-\kappa_{cell} \nabla T) = Q_{cell}$	Heat conduction in the cell and cooling plates
13	$Q_{cell} = A_{cell,c} \int_0^L \left(-\frac{\partial I_l \partial \phi_l}{\partial x \partial x} - \frac{\partial I_s \partial \phi_s}{\partial x \partial x} + a_v i_{loc} \eta\right) dL + I_{chrg}{}^2 R_{cc}$	Total heat generation rate from cell charging
14	$m_{clnt} C_{p,clnt} \frac{dT_{clnt}}{dt} = 2 \iint^{A_{cell,a}} q_{clnt} dA - F R_{clnt} C_{p,clnt}(T_{clnt} - T_{clnt0})$	Heat conduction in coolant

Table S2. Boundary conditions for 1D electrochemical model and 3D thermal model.

Equation No.	Expression	Description
1D Electrochemical Model Boundary Conditions		
15	$-D_{l,eff}\left.\frac{\partial c_l}{\partial x}\right\|_{x=0;\,x=L}=0$	No flux at anode current collectors (x=0) and cathode current collector (x=L).
16	$\phi_s\|_{x=0}=0$	Electric ground at anode current collector
17	$i_s\|_{x=L}=i_{chrg}$	Charging current control
18	$\phi_s\|_{x=L}=E_{cell,\,lim}$	Constant voltage holding
19	$\left.\frac{\partial c_s}{\partial r}\right\|_{r=0}=0$	No flux at particle radial center
20	$-D_s\left.\frac{\partial c_s}{\partial r}\right\|_{r=r_p}=\frac{i_{loc}\,r_p}{F\;3\varepsilon_s}$	Flux at particle reaction surface
21	$i_{\eta,lim}=i_{chrg}\left(1+K_{\eta,p}^{PID}(\eta_{min}-\eta_{pp})+K_{\eta,d}^{PID}\left(\frac{\partial\eta_{min}}{\partial t}\right)\right)$	PID plating protection current control
22	$i_{T,lim}=\frac{\left\|i_{chrg}(\nabla\cdot(\kappa_{cell}\nabla T))\right\|}{\|q_{tot}\|}\left(1-K_{T,p}^{PID}(T_{max}-T_{max,lim})-K_{T,d}^{PID}\left(\frac{\partial T_1}{\partial}\right.\right.$	PID thermal protection current control
3D Thermal Model Boundary Condition		
23	$-a\cdot q_{clnt}=h_{cell,a}(T_{clnt}-T\|_{cell,a})$	Cooling surface heat flux (No flux at other surfaces)

Table S3. Model input parameters and their values/expression.

Property	Unit	Symbol	Value/Expression	Reference
Anode Parameters (A12 graphite)				
Diffusion coefficient	$m^2 \cdot s^{-1}$	D_s	5.00×10^{-14}	5
Exchange current density	$A \cdot m^{-2}$	$i_{0,ref}$	16.43	5
Diffusion activation energy	$kJ \cdot mol^{-1}$	$E_{a,D}$	30	6
Exchange current activation energy	$kJ \cdot mol^{-1}$	E_{a,i_0}	59.1	7
Heat capacity	$J \cdot (kg \cdot K)^{-1}$	C_p	750	8
Thermal conductivity	$W \cdot (m \cdot K)^{-1}$	κ	2.36	9
Electrode conductivity	$S \cdot m^{-1}$	σ_s	50	fit
Specific surface area	m^{-1}	a_v	3.30×10^5	5
Porosity	–	ε_l	0.3	5
Particle radius	μm	r_p	5.15	5
Bruggeman exponent	–	p	2.4	5
Cathode Parameters (NMC532)				
Diffusion coefficient	$m^2 \cdot s^{-1}$	D_s	6.90×10^{-15}	5
Exchange current density	$A \cdot m^{-2}$	$i_{0,ref}$	2.02	5
Diffusion activation energy	$kJ \cdot mol^{-1}$	$E_{a,D}$	30	6
Exchange current activation energy	$kJ \cdot mol^{-1}$	E_{a,i_0}	60.8	7
Heat capacity	$J \cdot (kg \cdot K)^{-1}$	C_p	800	8
Thermal conductivity	$W \cdot (m \cdot K)^{-1}$	κ	1.03	9
Electrode conductivity	$S \cdot m^{-1}$	σ_s	10	fit
Specific surface area	m^{-1}	a_v	8.20×10^5	5
Porosity	–	ε_l	0.35	5
Particle radius	μm	r_p	1.8	5
Bruggeman exponent	–	p	2	5
Electrolyte Parameters (Gen2 - 1.2 M $LiPF_6$, EC:EMC 3:7) (c_l: $mol \cdot L^{-1}$, T: K)				
Diffusion coefficient	$cm^2 \cdot s^{-1}$	D_l	$0.00584e^{\left(-\frac{2870}{T}\right)}c_l^2 - 0.033$	10

Conductivity	$S \cdot cm^{-1}$	σ_l	$0.0345e^{\left(-\frac{798}{T}\right)}c_l^3 - 0.485e^{\left(-$	10
Transference number	–	t_+	$-0.000267e^{\left(\frac{883}{T}\right)}c_l^2 - 0.003$	10
Activity coefficient	–	$f_\pm$	$0.540e^{\left(\frac{329}{T}\right)}c_l^2 - 0.00225e^{\left(\frac{1}{-}\right.}$	10
Separator Parameters (Celgard 2325)				
Porosity	–	ε_l	0.39	5
Bruggeman exponent	–	p	2.5	5
Heat capacity	$J \cdot (kg \cdot K)^{-1}$	C_p	1800	11
Thermal conductivity	$W \cdot (m \cdot K)^{-1}$	κ	0.5	11

Table S4. Parameters/variables and their description.

Symbol	Description	Symbol	Description
a	Unit vector of Cell type-'a' surface in contact with cooling plate	i_{loc}	Local electrochemical reaction current density
a_v	Specific surface area	i_l	Ionic current density
$A_{cell,\,a}$	Cell type-'a' surface area, in contact with cooling plate	I_l	Ionic current
$A_{cell,\,c}$	Cell type-'c' surface area, cross-sectional	i_s	Electronic current density
α_a	Anode reaction transfer coefficients	I_s	Electronic current
α_c	Cathode reaction transfer coefficients	$i_{\eta,lim}$	PID plating protection current density
C_{dl}	Double layer capacitance	$i_{T,lim}$	PID thermal protection current density
c_l	Electrolyte salt concentration	κ	Thermal conductivity
$c_{l,ref}$	Electrolyte reference salt concentration	$K_{\eta,d}^{PID}$	PID derivative term coefficient for plating protection current control
c_s	Li-ion concentration in active material	$K_{\eta,p}^{PID}$	PID proportional term coefficient for plating protection current control
$c_{s,max}$	Li-ion maximum concentration in active material	$K_{T,d}^{PID}$	PID derivative term coefficient for thermal protection current control
$c_{s,ref}$	Li-ion reference concentration in active material $c_{s,ref} = c_{s,max}/2$	$K_{T,p}^{PID}$	PID proportional term coefficient for thermal protection current control
C_p	Heat capacity	L	Cell tri-layer unit cell thickness
D_l	Effective salt diffusion coefficient in electrolyte	m_{cell}	Cell mass
D_s	Lithium diffusion coefficient in bulk active material	ϕ_l	Electrolyte potential
$E_{a,D}$	Diffusion activation energy	ϕ_s	Potential of electronically conducting matrix
E_{a,i_0}	Exchange current activation energy	Q_{cell}	Cell total heat generation power
$E_{cell,lim}$	Cell voltage upper limit	q_{clnt}	Cell areal heat removal power by coolant
E_0^{eq}	Equilibrium potential reference	R	Universal gas constant
ε_l	Electrolyte volume fraction	R_{cc}	Total resistance of current collector
ε_s	Electrode volume fraction	r	Particle radial coordinate in active material
η	Overpotential	r_p	Particle radius
η_{min}	Cell minimum plating overpotential	σ_l	Electrolyte conductivity

η_{PP}	Li plating overpotential cutoff	σ_s	Electrode electronic conductivity
F	Faraday's constant	t	Time
$f_{\pm}$	Electrolyte salt activity coefficient	t_+	Cation transference number
FR_{clnt}	Coolant flow rate	T_{avg}	Cell average temperature
$h_{cell,a}$	Heat transfer coefficient at cell type-'a' surfaces	T_{clnt}	Coolant temperature
i_0	Exchange current density	T_{clnt0}	Initial and incoming channel coolant temperature
$i_{0,ref}$	Reference exchange current density	T_{max}	Cell maximum temperature
I_{chrg}	Charging current	$T_{max,lim}$	Cell maximum temperature upper limit
i_{chrg}	Charging current density	T_{min}	Cell minimum temperature
i_{dl}	Double layer current density	x	Cell coordinate

Number of Layers in Cell	Cathode Thickness (µm)	Anode Thickness (µm)	Cell Capacity (Ah)	Cell Energy (Wh)	Cell Mass (kg)	Cell Volume (L)	Specific Energy, (Wh/kg)	Energy Density, (Wh/L)
50	169.3	197.5	132.2	476	1.81	0.69	263.4	693.2
55	152.5	177.9	131.0	473	1.81	0.69	261.0	687.6
60	138.5	161.6	129.9	469	1.81	0.69	258.7	682.7
65	126.7	147.8	128.7	465	1.82	0.69	256.2	676.8
70	116.6	136.0	127.5	462	1.82	0.69	253.8	671.5
75	107.8	125.8	126.3	458	1.82	0.69	251.2	665.4
80	100.1	116.8	125.1	454	1.82	0.69	248.7	660.0
85	93.3	108.9	123.9	450	1.83	0.69	246.2	653.8
90	87.3	101.8	122.7	446	1.83	0.69	243.6	648.2
100	77.0	89.9	120.3	437	1.83	0.69	238.5	636.2
110	68.6	80.1	118.0	429	1.84	0.69	233.4	624.1
120	61.7	71.9	115.6	421	1.84	0.69	228.2	611.9
130	55.7	65.0	113.2	412	1.85	0.69	223.0	599.6
140	**50.7**	**59.1**	**110.8**	**404**	**1.85**	**0.69**	**217.9**	**587.3**
150	46.3	54.0	108.4	395	1.86	0.69	212.7	574.9
160	42.4	49.5	106.1	387	1.86	0.69	207.6	562.5
170	39.0	45.5	103.7	378	1.87	0.69	202.4	550.0
180	36.0	42.0	101.3	369	1.87	0.69	197.3	537.6
190	33.3	38.9	98.9	361	1.88	0.69	192.2	525.1
200	30.9	36.1	96.5	352	1.88	0.69	187.2	512.5
220	26.7	31.2	91.8	335	1.89	0.69	177.1	487.3
240	23.2	27.1	87.0	318	1.90	0.69	167.1	462.2
260	20.3	23.6	82.3	301	1.91	0.69	157.2	437.0
280	17.7	20.7	77.5	283	1.92	0.69	147.4	411.9
300	15.5	18.1	72.8	266	1.93	0.69	137.6	386.7

Table S5. Corresponding capacities and masses for a simulated cell

Supplementary References

1. Kim, G.-H., Smith, K., Lawrence-Simon, J., and Yang, C. (2016). Efficient and Extensible Quasi-Explicit Modular Nonlinear Multiscale Battery Model: GH-MSMD. J. Electrochem. Soc. *164*, A1076–A1088.

2. Doyle, M., Fuller, T.F., and Newman, J. (1993). Modeling of Galvanostatic Charge and Discharge of the Lithium/Polymer/Insertion Cell. J. Electrochem. Soc. *140*, 1526–1533.

3. Kim, H.-K., Kim, C.-J., Kim, C.-W., and Lee, K.-J. (2018). Numerical analysis of accelerated degradation in large lithium-ion batteries. Comput. Chem. Eng. *112*, 82–91.

4. Paul A. Nelson, Kevin G. Gallagher, Shabbir Ahmed, Dennis W. Dees, Naresh Susarla, Ira D. Bloom, Joseph J. Kubal, Juhyun Song, Zhe Liu BatPaC (Battery Performance and Cost) Software. Argonne National Laboratory. https://www.anl.gov/cse/batpac-model-software.

5. Colclasure, A.M., Dunlop, A.R., Trask, S.E., Polzin, B.J., Jansen, A.N., and Smith, K. (2019). Requirements for Enabling Extreme Fast Charging of High Energy Density Li-Ion Cells while Avoiding Lithium Plating. Journal of The Electrochemical Society *166*, A1412–A1424.

6. Ji, Y., Zhang, Y., and Wang, C.-Y. (2013). Li-Ion Cell Operation at Low Temperatures. J. Electrochem. Soc. *160*, A636–A649.

7. Keefe, A.S., Buteau, S., Hill, I.G., and Dahn, J.R. (2019). Temperature Dependent EIS Studies Separating Charge Transfer Impedance from Contact Impedance in Lithium-Ion Symmetric Cells. J. Electrochem. Soc. *166*, A3272.

8. Loges, A., Herberger, S., Seegert, P., and Wetzel, T. (2016). A study on specific heat capacities of Li-ion cell components and their influence on thermal management. J. Power Sources *336*, 341–350.

9. Loges, A., Herberger, S., Werner, D., and Wetzel, T. (2016). Thermal characterization of Li-ion cell electrodes by photothermal deflection spectroscopy. J. Power Sources *325*, 104–115.

10. Dees, D., Gunen, E., Abraham, D., Jansen, A., and Prakash, J. (2008). Electrochemical Modeling of Lithium-Ion Positive Electrodes during Hybrid Pulse Power Characterization Tests. J. Electrochem. Soc. *155*, A603.

11. Vishwakarma, V., and Jain, A. (2014). Measurement of in-plane thermal conductivity and heat capacity of separator in Li-ion cells using a transient DC heating method. J. Power Sources *272*, 378–385.